Iron impurities in gold and silver: Comparison of transport measurements to numerical renormalization group calculations exploiting non-Abelian symmetries

M. Hanl,[1] A. Weichselbaum,[1] T. A. Costi,[2] F. Mallet,[3] L. Saminadayar,[3,4] C. Bäuerle,[3] and J. von Delft[1]

[1]*Physics Department, Arnold Sommerfeld Center for Theoretical Physics and Center for NanoScience, Ludwig-Maximilians-Universität München, 80333 München, Germany*

[2]*Peter Grünberg Institut and Institute for Advanced Simulation, Research Centre Jülich, 52425 Jülich, Germany*

[3]*Institut Néel-CNRS and Université Joseph Fourier, 38042 Grenoble, France*

[4]*Institut Universitaire de France, 103 boulevard Saint-Michel, 75005 Paris, France*

(Received 18 May 2013; revised manuscript received 1 August 2013; published 30 August 2013)

We consider iron impurities in the noble metals gold and silver and compare experimental data for the resistivity and decoherence rate to numerical renormalization group results. By exploiting non-Abelian symmetries, we show improved numerical data for both quantities as compared to previous calculations [Costi *et al*., Phys. Rev. Lett. **102**, 056802 (2009).], using the discarded weight as criterion to reliably judge the quality of convergence of the numerical data. In addition, we also carry out finite-temperature calculations for the magnetoresistivity of fully screened Kondo models with $S = \frac{1}{2}$, 1, and $\frac{3}{2}$, and compare the results with available measurements for iron in silver, finding excellent agreement between theory and experiment for the spin-$\frac{3}{2}$ three-channel Kondo model. This lends additional support to the conclusion of Costi *et al*. that the latter model provides a good effective description of the Kondo physics of iron impurities in gold and silver.

DOI: 10.1103/PhysRevB.88.075146 PACS number(s): 73.23.−b, 72.70.+m, 75.20.Hr

I. INTRODUCTION

The magnetic alloys for which the Kondo effect was first observed, in the 1930s, were iron impurities in gold and silver.[1,2] They showed an anomalous rise in the resistivity with decreasing temperature, which Kondo explained in 1964 as being due to an antiferromagnetic exchange coupling between the localized magnetic impurity spins and the spins of the delocalized conduction electrons.[3] For his work, Kondo used a spin-$\frac{1}{2}$, one-band model, which undoubtedly captures the essential physics correctly in a qualitative way.

However, detailed comparisons between theory and experiment have since shown that this model does not yield a *quantitatively* correct description of the Kondo physics of dilute Fe impurities in Au or Ag. Such a description must meet the challenge of quantitatively reproducing, using the Kondo temperature T_K as only fitting parameter, several independent sets of experimental measurements: the contributions by magnetic impurities (indicated by a subscript m) to the temperature and field dependencies of the resistivity, $\rho_m(T,B)$, and to the temperature dependence of the decoherence rate, $\gamma_m(T)$, extracted from weak (anti)localization measurements. The spin-$\frac{1}{2}$, 1-band Kondo model does not meet this challenge: when comparing its predictions, obtained by the numerical renormalization group (NRG),[4–6] to transport measurements on dilute Fe impurities in Ag wires, different Kondo scales were required for fitting the resistivity and decoherence rates.[7,8]

In a recent publication (Ref. 9, involving most of the present authors, henceforth referred to as paper I), it was argued that the proper effective low-energy Kondo model for Fe in Au or Ag is, in fact, a fully screened, spin-$\frac{3}{2}$ three-channel Kondo model. Paper I arrived at this conclusion by the following chain of arguments. Previous transport experiments[7,8] had indicated that these systems are described by a fully screened Kondo model,[10–14] i.e., a Kondo model in which the local spin S is related to the number of conduction bands n by $S = n/2$. As mentioned above, the choice $n = 1$ had already been ruled out in earlier work.[7,8] Density-functional theory calculations for Fe in Au and Ag, presented in paper I, showed that in these host metals Fe preferentially acts as a substitutional defect with cubic symmetry, leading to a substantial crystal field splitting ($\geqslant$0.15 eV) between a higher-lying e_g doublet and a lower-lying t_{2g} triplet. Moreover, the local spin moment was predicted to be 3 Bohr magnetons, with an almost fully quenched orbital angular momentum. This suggested a fully screened Kondo model with $n = 3$ as the most likely candidate, while leaving some scope for the possibility of $n = 2$ (but none for $n = 4$ or 5). To discriminate between the options $n = 2$ and 3, $\rho_m(T,0)$ and $\gamma_m(T)$ were then calculated using NRG, for $n = 1$ (as reference), 2 and 3. Next, for both material systems (Fe in Au and Ag), the $\rho_m(T,0)$ curves were fitted to experimental data to obtain a Kondo temperature, $T_K^{(n)}$, for each of the three models. Finally, using these $T_K^{(n)}$ values, the $\gamma_m(T)$ curves, which constituted parameter-free predictions of the decoherence rate, were compared to corresponding measurements, with the conclusion that the choice $n = 3$ worked distinctly better than $n = 2$.

The goal of the present paper is twofold. First, we describe technical details of the numerical calculations performed in paper I that could not be presented there for lack of space. Second and more important, we extend the analysis of paper I to the case of finite magnetic fields. Indeed, though experimental data for $\rho_m(T, B \neq 0)$ had been available for Fe in Ag even at the time of writing of paper I, it had not been possible then to compare them to theoretical predictions for $n = 3$. The reason is that multichannel calculations present an enormous challenge for the NRG, as the numerical complexity grows exponentially with the number of channels. In paper I, only Abelian symmetries (charge conservation in each channel and total spin S_z) were exploited. For the purposes of paper I, this turned out to be sufficient, but for the aforementioned three-channel Kondo model, the calculations were numerically extremely costly, and even at $B = 0$ just barely within the

limits of feasibility. When the present authors attempted, in subsequent work (unpublished), to treat the more general case of a finite magnetic field using the same approach, the latter turned out to be inadequate, plagued by numerical convergence issues. Therefore further progress required enhancing the numerical efficiency by exploiting non-Abelian symmetries.

Now, the effective fully screened symmetric three-channel Kondo model mentioned above has several *non*-Abelian symmetries, including, in particular, an SU(3) channel symmetry. This implies that the eigenspectrum of the Hamiltonian can be organized into degenerate symmetry multiplets, and great gains in numerical efficiency can be made by exploiting this multiplet structure at every step of the NRG procedure. We took this observation as incentive to implement non-Abelian symmetries in our code on a completely generic footing for tensor networks such as the NRG.[15] Although the exploitation of symmetries, Abelian as well as non-Abelian, together with their respective strong gain in numerical efficiency is well known in the literature, the treatment of non-Abelian symmetries in NRG has been largely restricted to the symmetry of SU(2).[4,5,16,17] The non-Abelian symmetry SU(2), however, is simpler than the general case, since for $n \geqslant 3$ the SU(n) representation theory involves complications due to the presence of inner and outer multiplicities. A generic numerical framework for treating arbitrary non-Abelian symmetries thus had been missing, and became available only very recently.[15,18,19]

More specifically, the model Hamiltonians studied here possess SU(2) particle-hole symmetry, SU(n) channel symmetry, and SU(2) spin symmetry for $B = 0$ or Abelian S_z symmetry for $B \neq 0$. By exploiting the non-Abelian symmetries, we were able to drastically reduce the computational effort and generate fully converged numerical data, even for the highly challenging case of three channels. With a significantly more powerful NRG at our hands then, the following analysis serves two purposes. First, we present a thorough reanalysis of paper I with improved NRG data. In particular, we give a detailed discussion of NRG truncation and convergence issues, which are under much better control with the new non-Abelian scheme. The new numerical results show discernible quantitative differences w.r.t. paper I, leading to changes in the deduced Kondo temperatures that are quite substantial for $n = 3$ (the relative change in T_K is 31% for Fe in Au and 53% for Fe in Ag). Second, we present a detailed analysis of the new numerical magnetoresistivity data and compare these to experimental results for Fe in Ag. The results of both analyses fully confirm the main conclusion of paper I: the effective microscopic model for dilute iron impurities in the noble metals gold and silver is given by a fully screened three-channel Kondo model.

The remainder of this paper is organized as follows: Sec. II describes the model, Sec. III describes NRG-related details, and Sec. IV provides a comparison of experimental and numerical magnetoresistance data, followed by a summary in Sec. V.

II. MODEL

In paper I, we found it numerically convenient for our NRG calculations to start not from a pure Kondo model but from an effective Anderson-type model, because it is then possible to obtain an improved spectral function by using the so-called "self-energy trick,"[20] which involves calculating the impurity-level self-energy. It has recently been shown[21] that a similar strategy can be used for Kondo-type models, but this fact was brought to our attention only after completion of the present study.[22] We here adhere to the strategy of paper I and adopt the following Anderson-type model,

$$\hat{H} = \sum_{\alpha=1}^{n} \sum_{k\sigma} [t(\hat{d}^\dagger_{\alpha\sigma}\hat{c}_{k\alpha\sigma} + \text{H.c.}) + \varepsilon_k \hat{c}^\dagger_{k\alpha\sigma}\hat{c}_{k\alpha\sigma}] - J_{\text{H}}^{(n)} \hat{\vec{S}}^2_{\text{imp}} + g\mu_{\text{B}} B \hat{S}^z_{\text{imp}} , \quad (1)$$

which reduces to a Kondo-type model at low energies.[23,24] The index α labels n degenerate local levels as well as n independent channels of conduction electrons, each forming a flat band of half-bandwidth $D = 1$ with constant density of states $\nu_0 = 1/2D$ per spin and channel. (In the remainder of the paper, all energies are specified in units of half-bandwidth, unless indicated otherwise.) $\hat{d}_{\alpha\sigma}$ is the annihilation operator of an impurity electron with spin σ in level α, whereas $\hat{c}_{k\alpha\sigma}$ annihilates a reservoir electron in channel α with wave number k and energy ε_k. Levels and channels are tunnel-coupled diagonally in spin and channel indices, resulting in a width $\Gamma = \pi\nu_0 t^2$ for each level, t being the hopping matrix element between impurity and reservoir. The third term in $\hat{H}$ describes a Hund-type exchange interaction with $J_{\text{H}}^{(n)} > 0$, added to favor a local spin of $S = n/2$, where $\hat{\vec{S}}_{\text{imp}} = \sum_{\alpha=1}^{n} \hat{\vec{S}}_\alpha$ is the total impurity spin operator, $\hat{\vec{S}}_\alpha = \frac{1}{2}\sum_{\sigma\sigma'} \hat{d}^\dagger_{\alpha\sigma'}\vec{\tau}_{\sigma'\sigma}\hat{d}_{\alpha\sigma}$ is the spin operator for an electron in level α, and $\vec{\tau} = (\tau_x, \tau_y, \tau_z)$ are Pauli spin matrices. The last term in $\hat{H}$ describes the effect of an applied local magnetic field, with $g = 2$. To ensure particle-hole symmetry (which renders the numerics more efficient), we take $\varepsilon_{\alpha\sigma} = 0$ for the local level positions and do not include any further charging energy.

The energies of the free orbital (FO) states are given by roughly $J_{\text{H}}^{(n)} S(S+1)$ and the energy difference between two FO states that differ by spin $\frac{1}{2}$ is therefore given by $\Delta E^{(n)} \approx J_{\text{H}}^{(n)}[S(S+1) - (S-\frac{1}{2})(S+\frac{1}{2})] = J_{\text{H}}^{(n)}(S+\frac{1}{4})$. To focus on the local moment regime of the Anderson model, we choose $J_{\text{H}}^{(n)}$ such that $\Delta E^{(n)}$ is significantly larger than Γ and $g\mu_{\text{B}}B$, ensuring a well-defined local spin of $S = n/2$, and an average total occupancy of the local level of $\sum_{\alpha\sigma}\langle \hat{d}^\dagger_{\alpha\sigma}\hat{d}_{\alpha\sigma}\rangle = n$. Moreover, the ratios $J_{\text{H}}^{(n)}/\Gamma$ are chosen such that the resulting Kondo temperatures have comparable magnitudes. In paper I, we had implemented this strategy using the same $\Delta E^{(n)}$ for all three n values, with $\Gamma = 0.01$ and $J_{\text{H}}^{(1)} = 0.053$, $J_{\text{H}}^{(2)} = 0.032$, $J_{\text{H}}^{(3)} = 0.023$. We have since realized that much better NRG convergence properties can be obtained by choosing much larger values of $J_{\text{H}}^{(n)}$, to ensure that the energy differences of the FO states truly lie well above the bandwidth ($\Delta E^{(n)} \gtrsim 100$). This is the numerical counterpart to the Schrieffer-Wolff transformation:[15,25] it shifts the numerically most expensive, yet irrelevant, FO regime to an energy range that lies outside the range whose energies are finely resolved during the NRG diagonalization, thus reducing the numerical costs needed for treating the Anderson model to a level comparable to that of the Kondo model. For the numerical calculations presented

here, we set the level width to $\Gamma = 25$ and choose $J_{\rm H}^{(n)}$ such that the resulting spectral functions have the same half-width at half maximum ($=2\times10^{-4}$) for all three cases, $n \in \{1,2,3\}$, thus ensuring that the Kondo temperatures are equal. This is achieved by choosing the Hund couplings as $J_{\rm H}^{(1)} = 358.9$, $J_{\rm H}^{(2)} = 112.8$, and $J_{\rm H}^{(3)} = 57.14$.

For the model in Eq. (1), the resistivity and decoherence rate due to magnetic impurities (relevant for weak localization) can be calculated as follows:[26,27]

$$\rho_{\rm m}^{\rm NRG}(T,B) = \frac{\rho_{\rm m}^0}{2n}\int d\omega f'(\omega)\sum_{\alpha\sigma}{\rm Im}\big(\Gamma G^R_{\alpha\sigma}(\omega)\big), \quad (2)$$

$$\gamma_{\rm m}^{\rm NRG}(T) = \left[\int d\omega(-f'(\omega))\sqrt{\gamma_{\rm m}(\omega,T)}\right]^2, \quad (3)$$

$$\gamma_{\rm m}(\omega,T) = -\frac{\gamma_{\rm m}^0}{2n}\sum_{\alpha\sigma}\left[{\rm Im}\big(\Gamma G^R_{\alpha\sigma}(\omega)\big) + \big|\Gamma G^R_{\alpha\sigma}(\omega)\big|^2\right]. \quad (4)$$

Here, $G^R_{\alpha\sigma}(\omega)$ is the fully interacting retarded impurity Green's function, $f'(\omega)$ is the derivative of the Fermi function, $\rho_{\rm m}(0) = \rho_{\rm m}^0 = 2\tau\bar\rho/\pi\hbar\nu_0$ and $\gamma_{\rm m}^0 = 2/\pi\hbar\nu_0$, where $\bar\rho$ is the resistivity due to static disorder and τ the corresponding elastic scattering time. For *real* materials with complex Fermi surfaces, both prefactors $\rho_{\rm m}^0$ and $\gamma_{\rm m}^0$ contain material-dependent (hence unknown) factors arising from integrals involving the true band structure of the conduction electrons.

III. NRG DETAILS

A. Wilson chain and spectral function

Within the NRG, the noninteracting bath in Eq. (1) is coarse grained using the dimensionless discretization parameter $\Lambda > 1$, followed by the mapping onto the so-called Wilson chain in terms of the fermionic Wilson sites[4–6] $\hat f_{i'\alpha\sigma}$ with $i' \in \{0,1,\ldots\}$. Therefore $\hat H \cong \lim_{N\to\infty}\hat H_N$, where

$$\hat H_N \cong \hat H_{\rm loc} + \sum_{i'=0}^{N-1} t_{i'}\sum_{\alpha=1}^{n}\sum_{\sigma}(\hat f^\dagger_{i',\alpha\sigma}\hat f_{i'+1,\alpha\sigma} + {\rm H.c.}) \quad (5a)$$

$$\hat H_{\rm loc} \equiv \hat H_{\rm J} + \sum_{\alpha=1}^{n}\sum_{\sigma}\sqrt{\tfrac{2\Gamma}{\pi}}(\hat d^\dagger_{\alpha\sigma}\hat f_{0\alpha\sigma} + {\rm H.c.}), \quad (5b)$$

where

$$\hat H_{\rm J} = -J_{\rm H}{}^{(n)}\hat{\vec S}^2_{\rm imp} + g\mu_{\rm B}B\hat S^z_{\rm imp}. \quad (5c)$$

The impurity spin is coupled to a semi-infinite tight-binding chain with the exponentially decaying couplings $t_{i'} \propto \Lambda^{-i'/2}$. For large enough $\Lambda \gtrsim 2$, this ensures energy scale separation, and thus justifies the iterative diagonalization of the Hamiltonian in the representation of the Wilson chain.[4–6] In particular, the energies of the Hamiltonian $\hat H_i$ at intermediate iterations that include all terms $i' < i$, are rescaled in units of ω_i, where

$$\omega_i \equiv a\Lambda^{-i/2}. \quad (6)$$

Here, the constant a is chosen such that $\lim_{i\to\infty} t_i/\omega_i = 1$. An analytic expression for a in the presence of z shifts is given in Ref. 28.

To obtain the Green's function $G^R_{\alpha\sigma}(\omega)$, which determines $\rho_{\rm m}^{\rm NRG}(T,B)$ and $\gamma_{\rm m}^{\rm NRG}(T)$, we calculate the spectral function $A_{\alpha\sigma}(\omega) = -\frac{1}{\pi}{\rm Im}(G^R_{\alpha\sigma}(\omega))$ using its Lehmann representation:

$$A_{\alpha\sigma}(\omega) = \sum_{a,b}\frac{e^{-\beta E_a}+e^{-\beta E_b}}{Z}|\langle a|\hat d_{\alpha\sigma}|b\rangle|^2\delta(\omega - E_{ab}), \quad (7)$$

where $E_{ab} = E_b - E_a$, with E_a, E_b and $|a\rangle$, $|b\rangle$ being the eigenenergies and many-body eigenstates obtained by NRG in the full density matrix (FDM) approach.[29–32] Note that due to the SU(n) symmetry of the Hamiltonian, the spectral function $A_{\alpha\sigma}(\omega)$ does not depend on the index α. Thus when exploiting non-Abelian symmetries, in practice, one calculates the channel-independent symmetrized spectral function $A_\sigma(\omega) \equiv \frac{1}{n}\sum_{\alpha=1}^n A_{\alpha\sigma}(\omega)$, which corresponds to the normalized scalar contraction $\hat d^\dagger_\sigma\cdot\hat d_\sigma \equiv \sum_\alpha \hat d^\dagger_{\alpha\sigma}\cdot\hat d_{\alpha\sigma}$ of the spinors $\hat d_\sigma$.[15]

For the calculation of $\gamma_{\rm m}(T)$, the knowledge of both the real and the imaginary part of $G^R_{\alpha\sigma}(\omega) \equiv G^R_\sigma(\omega)$ is necessary. The real part can be determined via the Kramers-Kronig relations from $A_\sigma(\omega)$ after smoothing the discrete data. $\rho_{\rm m}^{\rm NRG}(T,B)$, on the other hand, requires only the imaginary part of the Green's function. This makes the application of the Kramers-Kronig relations and with it the broadening of the discrete data unnecessary and $\rho_{\rm m}^{\rm NRG}(T,B)$ can therefore be directly calculated from the discrete data,[29] thus avoiding possible broadening errors. Furthermore, due to particle-hole symmetry, it is sufficient to calculate $A_\sigma(\omega)$ only for one spin σ, since the spectral functions for opposite spins σ and $\bar\sigma$ are symmetric with respect to each other: $A_\sigma(\omega) = A_{\bar\sigma}(-\omega)$.

B. Convergence criteria and discarded weight

As mentioned in the introduction, when using Abelian symmetries the calculations described above are standard for $n = 1$ and $n = 2$, but a real challenge for $n = 3$. The reason is that the number of degenerate eigenstates in a typical symmetry multiplet increases strongly with the rank of the symmetry group. For example, for the present model with $n = 3$, the typical degeneracy quickly becomes of order 10^2 to 10^3 even for low-lying energy multiplets (this is illustrated by the presence of long "plateaux" in the excitation spectra shown in Fig. 1). This implies that the number of kept states needs to increase dramatically, too. Moreover a crucial prerequisite for well-converged results is that the multiplet structure should be respected during NRG truncation. No multiplet should be kept only partially, i.e., cut in two; instead, each multiplet should be kept or discarded as a whole. In the present paper, cutting multiplets is avoided by implementing non-Abelian symmetries explicitly and keeping all multiplets below a specified truncation energy, as described further below. In paper I, which implemented only Abelian symmetries, we had used the more conventional NRG truncation scheme of specifying the total maximum number of states to typically be kept. However, we had adjusted this number as needed to ensure that the lowest-lying discarded states were not degenerate with the highest-lying kept states. Moreover, the energy of the highest kept multiplet turned out to lie just below a wide gap in the energy spectrum [see Fig. 1(a)]. In our subsequent work, we have found that the presence of this wide gap considerably stabilizes the results; when we keep some more multiplets such that the highest ones lie just

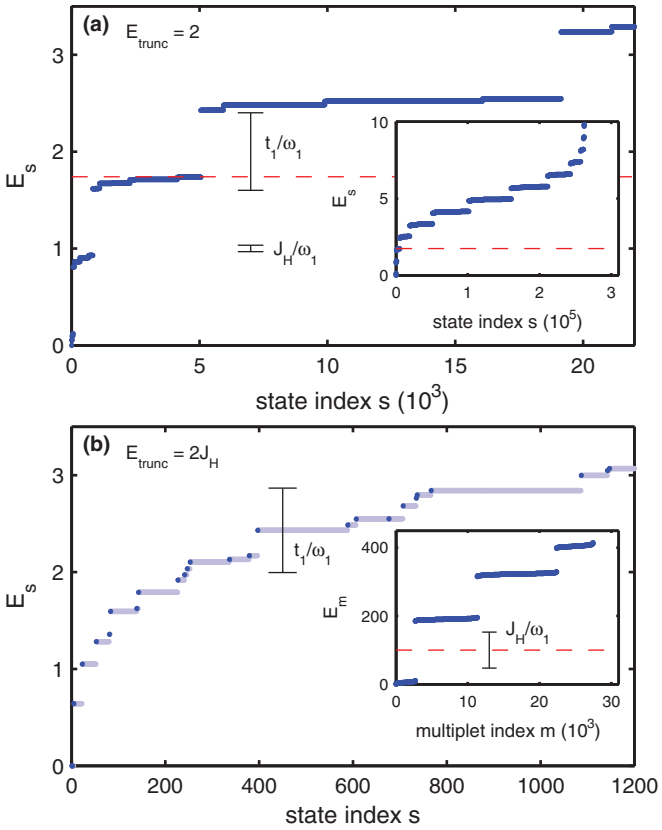

FIG. 1. (Color online) Eigenenergies of the $n = 3$ calculations from (a) paper I and (b) this work, for the lowest eigenstates (blue circles) and truncation energy (dashed red line) of NRG iteration $i = 1$. This iteration includes the impurity and the first two Wilson sites $\hat{f}_0$ and $\hat{f}_1$, which by Eq. (5a) corresponds to $\hat{H}_1$; it is the first iteration where truncation occurred. All energies E_s are given in units of ω_1 [cf. Eq. (6)]. In (a), each dark blue dot marks an eigenstate; in (b), each dark blue dot marks a multiplet, whose degeneracy is indicated by the length of the adjacent light blue lines. Dashed red lines indicate the truncation energy E_{trunc}. In paper I, the number of kept states at iteration $i = 1$ was 4840 which was 216 states short of truncating into the wider energy gap starting at $E_s = 5056$. For the present paper, we chose the truncation energy to lie well within a wide spectral gap and kept 16 384 out of 262 144 states [only a small subset of which are shown in the main panel of (b)]. This large number was achievable by grouping the kept states into 2688 symmetry multiplets with internal degeneracy. The insets of (a) and (b) show, respectively, the full spectrum of states or multiplets at iteration $i = 1$. (The fine structure seen in the main panel in (b) is not resolved in the inset, since the latter uses a much coarser energy resolution on the vertical axis.) The spectra in (a) and (b) have different fine structure, because the model parameters were chosen differently in paper I and the present work, respectively: the former used $J_{\text{H}}^{(3)} = 0.0229$, $\Gamma = 0.01$, the latter $J_{\text{H}}^{(3)} = 57.14$, $\Gamma = 25$. As a result, the energy separation between degenerate multiplets at the truncation energy is different, namely $\mathcal{O}(t_1/\omega_1)$ in (a) versus $\mathcal{O}(J_{\text{H}}^{(n)}/\omega_1)$ in (b), where t_1 is the hopping matrix element between the first two sites of the Wilson chain [cf. Eq. (5a)]. The different values of J_{H} and t_1 used in (a) and (b) are indicated by black lines in the plots.

above the wide gap, the results deteriorate considerably, as judged by the criterion discussed next. The criterion used in paper I to judge the quality of convergence was based on the Friedel sum rule,[33] which for the present model implies that the Kondo peak of the zero-temperature spectral function should satisfy $\pi\Gamma \cdot A_{\alpha\sigma}(\omega = 0) = 1$. For paper I, this check was satisfied to within 2% for spectral functions calculated using the self-energy trick, which we had taken as indication that the data could be trusted. When calculated *without* the self-energy trick, though, the Kondo peak height was off by 1%, 16%, and 32% for $n = 1$, 2, and 3, respectively, which, in retrospect, indicates lack of full convergence for the latter two cases. Indeed, this became apparent *a posteriori* in the course of the present study when we reanalyzed the NRG data of paper I using a more reliable tool for checking NRG convergence that had been developed in 2011,[28] based on monitoring the discarded weight. In essence, the discarded weight measures the relevance of the highest-lying kept states for obtaining an accurate description of the ground state space a few iterations later. More concretely, it is calculated as follows: construct a reduced density matrix for a chain of length i from the mixed density matrix of the ground state space of a chain of length $i + i_0$ by tracing out the last i_0 sites (typically $i_0 \gtrsim 4$ to ensure that all eigenvalues of the reduced density matrix are nonzero); find the eigenvalues and eigenstates of this reduced density matrix, say $\rho_r^{[i;i_0]}$ and $|r_{i;i_0}\rangle$, and sort them according to their energy expectation values, $E_r^{[i;i_0]} = \langle r_{i;i_0}|\hat{H}_i|r_{i;i_0}\rangle$. The weight $\varepsilon_{5\%,i}^{\text{D}} \cong \sum_r^{\text{top }5\%} \rho_r^{[i;i_0]}$ contributed by the highest-lying 5% of states in this energy-sorted list then provides an estimate for the discarded weight at iteration i. It provides a quantitative measure for the importance of the discarded states had they been included in the description of the ground state space of iteration $i + i_0$ by keeping a larger number of states. Repeating this analysis for different sites i, the largest $\varepsilon_{5\%,i}^{D}$ value is taken to define the "discarded weight" of the entire Wilson chain, $\varepsilon_{5\%}^{\text{D}} = \max_i(\varepsilon_{5\%,i}^{D})$. The entire analysis concerns the kept space only, hence it is fast relative to the actual NRG calculation itself. Well-converged physical quantities are obtained when the discarded weight satisfies $\varepsilon_{5\%}^{\text{D}} \lesssim 10^{-10}$. For the NRG data used in paper I, the discarded weight calculated *a posteriori* turned out to be 2.8×10^{-13}, 2.9×10^{-9}, and 8.3×10^{-7} for $n = 1$, 2, and 3, respectively. This indicates lack of proper convergence for $n = 2$, and especially for $n = 3$.

C. Truncation scheme for non-Abelian symmetries

For the calculations presented here, we therefore use an improved code, which also exploits non-Abelian symmetries.[15] Here, the idea is to make use of the fact that degenerate states can be gathered into symmetry multiplets. By the Wigner-Eckart theorem, matrix elements including states from the same multiplet are then related via Clebsch Gordan coefficients. Thus it is sufficient to keep track not of all individual states inside each multiplet, but only of entire multiplets, and to store only one reduced matrix element for each multiplet. This drastically reduces the size of the matrix that has to be diagonalized at an NRG iteration, with corresponding reductions in calculation times and memory requirements.

Our model possesses the following non-Abelian symmetries: SU(2) particle-hole, SU(2) spin (in the absence of magnetic field), and SU(n) channel symmetry. For many of our calculations, we need $B \neq 0$, in which case the SU(2) spin symmetry is reduced to an Abelian symmetry using

S_z. Moreover, particle-hole and channel symmetries do not commute in general, yet their combination generates the larger symplectic symmetry Sp($2n$) (see Ref. 15). This symmetry, which encompasses both particle-hole and channel symmetry, fully exhausts the model's symmetry; consequently, no degeneracies remain between different Sp($2n$) multiplets (a typical multiplet contains several hundreds up to several thousands of states). For the calculations presented in this work, using SU(n) [rather than Sp($2n$)] turned out to be sufficient. Here, we use SU(n) channel symmetry together with total charge for $n \in \{2,3\}$ and particle-hole symmetry for $n = 1$. The gain in numerical efficiency due to these symmetries is huge. For example, for $n = 3$, the largest SU(n) multiplets kept in our NRG calculations already reach dimensions of above 100. By exploiting these symmetries, calculation times as well as memory requirements are reduced by more than two orders of magnitude compared to those of paper I. As a consequence, the calculations presented here can be simply performed within a few hours on standard workstations.

We used an NRG discretization parameter of $\Lambda = 4$, and perform z averaging[34] with $N_z = 2$ (and $z \in \{0,0.5\}$) to minimize discretization artifacts.[35] For $n = 3$, the computationally most challenging case, we used the following truncation scheme. For the diagonalization of $H_0 \equiv \hat{H}_{\rm loc}$, all states were kept. For iteration $i = 1$, we used a truncation energy [given in rescaled units of $\omega_{i=1}$, cf. Eq. (6)] of $E_{\rm trunc} = 2J_{\rm H}/D > 7$. Figure 1(b) shows a subset of the corresponding kept eigenenergies and multiplet degeneracies, while Fig. 1(a) shows corresponding information for the calculations from paper I. The inset of Fig. 1(b) shows that *all* Kondo-like states of the Anderson model have been retained. For iterations $i \geqslant 2$, we used $E_{\rm trunc} = 7$, except for $z = 0.5$ at iteration $i = 2$, where we used $E_{\rm trunc} = 6$ to reduce computational costs due to the extraordinary large density of states at that iteration; this choice of parameters corresponds to keeping $\lesssim$10 000 multiplets ($\lesssim$77 000 states). Using this scheme, a single NRG run for $n = 3$ required about 40 GB of RAM and took on the order of 10 hours of calculation time on an 8-core processor. The subsequent calculation of the spectral function required a similar amount of time and 55 GB memory. The large number of kept multiplets then resulted in high numerical accuracy. In particular, the spectral functions calculated with and without using the improved self-energy, already agreed very well with each other, which clearly demonstrates fully converged numerical data. Having established this for a few representative cases, we proceeded to calculate the data presented below without using the self-energy trick.

D. Resistivity obtained by non-Abelian NRG

To compare the results obtained with our new approach with those of paper I, Fig. 2(a) shows the temperature dependence of the zero-field resistivity for $n = 1$, 2, and 3, computed using both Abelian NRG with self-energy trick as in paper I (dashed lines) and using our new non-Abelian NRG approach (solid lines), which produced truly well-converged results. We define the Kondo temperature $T_{\rm K}^{(n)}$ associated with a given numerical resistivity curve $\rho_{\rm m}^{\rm NRG}(T,0)$ by the condition

$$\rho_{\rm m}^{\rm NRG}\left(T_{\rm K}^{(n)},0\right) = \tfrac{1}{2}\rho_{\rm m}^{\rm NRG}(0,0)\ . \qquad (8)$$

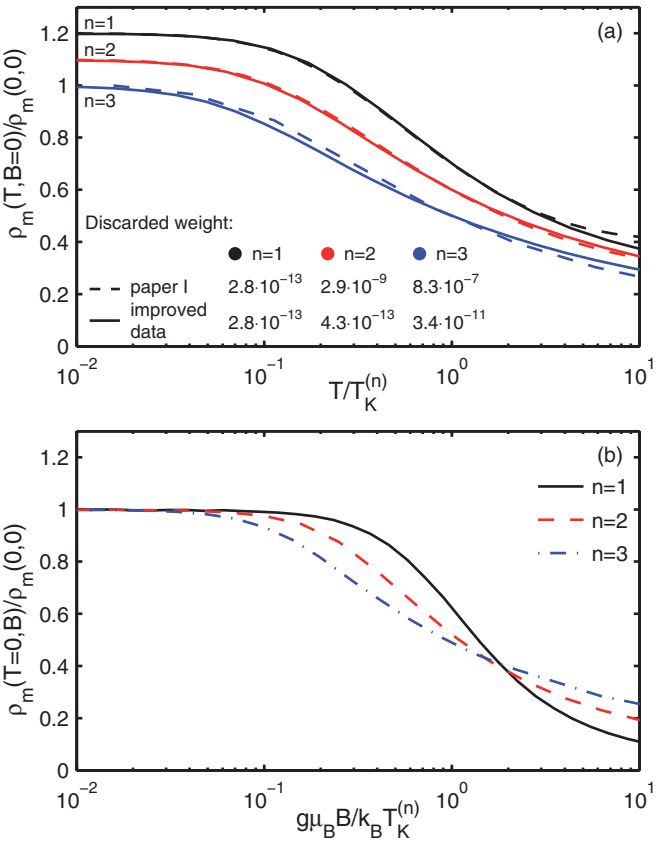

FIG. 2. (Color online) (a) Temperature dependence of the zero-field resistivity for $n = 1$, 2, and 3, computed using both Abelian NRG with self-energy trick as in paper I (dashed lines) and our new non-Abelian NRG approach (solid lines). For clarity, successive curves have been vertically shifted by 0.1. (b) The magnetic-field dependence of the zero-temperature resistivity for $n = 1$, 2, and 3, calculated using non-Abelian NRG.

Then $\rho_{\rm m}^{\rm NRG}(T,0)/\rho_{\rm m}^{\rm NRG}(0,0)$ versus $T/T_{\rm K}$ should be a universal curve for given n. For $n = 1$ and 2, the solid and dashed lines in Fig. 2(a) agree well (except at large temperatures for $n = 1$, where the dashed curve is affected by free-orbital states, implying that in paper I, $T_{\rm K}^{(1)}$ had not been chosen sufficiently small with respect to the FO excitation energy). For $n = 3$, however, the shapes of the dashed and solid curves actually differ quite noticeably. The reason for the difference is the lack of full convergence of the Abelian NRG data. This becomes clearly evident by comparing the discarded weights, listed in the legend of Fig. 2(a), of the non-Abelian and Abelian calculations: for $n = 3$, the respective discarded weights of 3.4×10^{-11} and 8.3×10^{-7} indicate that the former calculations, but not the latter, are well converged. This comparison thus highlights both the benefits of exploiting non-Abelian symmetries in order to reduce convergence problems, and the importance of checking the latter in a reliable fashion by monitoring the discarded weight.

The fact that the resistivity curve for $n = 3$ shows a more gradual decrease with increasing temperature for the new non-Abelian results than for the old Abelian ones, implies that fits to experiment will yield a larger Kondo temperature for the former, as we indeed find below.

TABLE I. Values of parameters determined from fitting the experimental measurement. The values for $T_K^{(n)}$ and $\delta^{(n)}$ are extracted using the fitting procedure whose results are shown in Fig. 3. $\Delta\rho^{\rm exp}(0,0)$ is the measured value for the resistivity at zero magnetic field and the lowest temperature avalaible. For the sake of completeness, we also show $\rho_{\rm m}^{{\rm uni},(n)}(0,0) = \Delta\rho^{\rm exp}(0,0) - \delta^{(n)}$, which, according to Eq. (10), corresponds to the unitary Kondo resistivity.

	n	AuFe3	AgFe2	AgFe3
$T_K^{(n)}$ (K)	1	0.6 ± 0.1	2.5 ± 0.2	2.8 ± 0.2
	2	1.0 ± 0.1	4.3 ± 0.3	4.7 ± 0.3
	3	1.7 ± 0.1	7.4 ± 0.5	8.2 ± 0.5
$\delta^{(n)}$ (nΩcm/ppm)	1	−0.002	0.003	0.001
	2	−0.045	−0.005	−0.007
	3	−0.090	−0.013	−0.016
$\Delta\rho^{\rm exp}(0,0)$ (nΩcm/ppm)		0.211	0.041	0.041
$\rho_{\rm m}^{{\rm uni},(n)}(0,0)$ (nΩcm/ppm)	1	0.213	0.038	0.040
	2	0.256	0.046	0.048
	3	0.301	0.054	0.057

Figure 2(b) shows the zero-temperature magnetoresistivity curves for $n = 1$, 2, and 3, calculated by non-Abelian NRG. The curves are scaled by the same $T_K^{(n)}$ as derived from the temperature-dependent data where the latter, by construction, cross at $T = T_K^{(n)}$ [cf. Eq. (8)]. Interestingly, the magnetic-field dependent curves here also approximately cross a common point at a magnetic field of about $g\mu_B B \sim 1.8\, k_B T_K^{(n)}$ having $\rho_m(T = 0, B)/\rho_m(0,0) \simeq 0.4$. The general trend of the curves in Fig. 2(b) is similar to that seen in Fig. 2(a): the larger n the more gradual the decrease in resistivity with increasing temperature or field. This indicates that the larger the local spin $S = n/2$, the larger the energy range (in units of $T_K^{(n)}$) within which its spin-flip-scattering effects are felt strongly by conduction electrons. In absolute energy units, this tendency is even stronger, since the fits to experiment performed below yield $T_K^{(1)} < T_K^{(2)} < T_K^{(3)}$ (cf. Table I). Interestingly, the n-dependent differences in curve shapes are more pronounced for the field dependence than for the temperature dependence;[36] in Fig. 2(b), the decrease of the resistivity for a given n sets in at a higher energy and then is steeper than in Fig. 2(a). Thus the comparison between experiment and theory for the magnetoresistivity performed below constitutes a stringent test of which choice of n is most appropriate, independent of and complementary to the tests performed in paper I.

IV. COMPARISON WITH EXPERIMENT

To identify the microscopic model that describes the system of iron impurities in gold and silver correctly, we compare NRG calculations for the resistivity $\rho_{\rm m}^{\rm NRG}(T,B)$ and the decoherence rate $\gamma_{\rm m}^{\rm NRG}(T)$ to experimental data, $\rho_{\rm m}^{\rm exp}(T,B)$ and $\gamma_{\rm m}^{\rm exp}$. [In the following, when referring to both NRG and experiment, we omit the upper index and write $\rho_{\rm m}(T,B)$ and $\gamma_{\rm m}(T)$.] The data to be analyzed stem from a detailed experimental study[7] performed in 2006 on quasi-one-dimensional wires. One AuFe sample and two AgFe samples were studied, to be denoted by AuFe3, AgFe2, and AgFe3, with impurity concentrations of 7 ± 0.7, 27 ± 3, and 67.5 ± 7 ppm, respectively. These concentrations are so small that multi-impurity effects can be ignored. Low-field measurements of the temperature-dependence of the resistivity, performed at $B = 0.1$ T to suppress weak localization, are available for all three samples. We will denote this data by $\rho_{\rm m}^{\rm exp}(T,0)$ [rather than $\rho_{\rm m}^{\rm exp}(T,0.1{\rm T})$], and compare it to numerical results for $\rho_{\rm m}^{\rm NRG}(T,0)$ computed at $B = 0$, since $1 - \rho_{\rm m}^{\rm NRG}(T,0.1{\rm T})/\rho_{\rm m}^{\rm NRG}(T,0) < 0.5\%$ for all three cases $n \in \{1,2,3\}$. Moreover, experimental data are available for $\gamma_{\rm m}^{\rm exp}(T)$ from AgFe2 and AuFe3, and for $\rho_{\rm m}^{\rm exp}(T,B)$ from AgFe2.

The comparison between experiment and theory proceeds in three steps. (i) First, we compare measured data and NRG predictions for the resistivity at zero magnetic field $\rho_{\rm m}(T, B = 0)$ to determine two fit parameters, $T_K^{(n)}$ and $\delta^{(n)}$, for each of the samples and each of the three models $n \in \{1,2,3\}$. After the fit parameters have been determined, we use $T_K^{(n)}$ and $\delta^{(n)}$ to make parameter-free predictions for (ii) the decoherence rate $\gamma_{\rm m}(T)$ and (iii) the temperature-dependent magnetoresistivity $\rho_{\rm m}(T,B)$, and compare these to experiment for those samples for which corresponding data is available. Here, (i) and (ii) represent a thorough reanalysis of the experimental data of paper I using our new, improved numerical data, while (iii) involves experimental data not published previously, and new numerical data.

A. Determination of fit parameters

The experimental resistivity data to be discussed below (shown in Fig. 3) have several contributions of different physical origin:

$$\Delta\rho^{\rm exp}(T,B) = \rho_{\rm m}^{\rm exp}(T,B) + \rho_{\rm ph}(T) + \delta\,. \qquad (9)$$

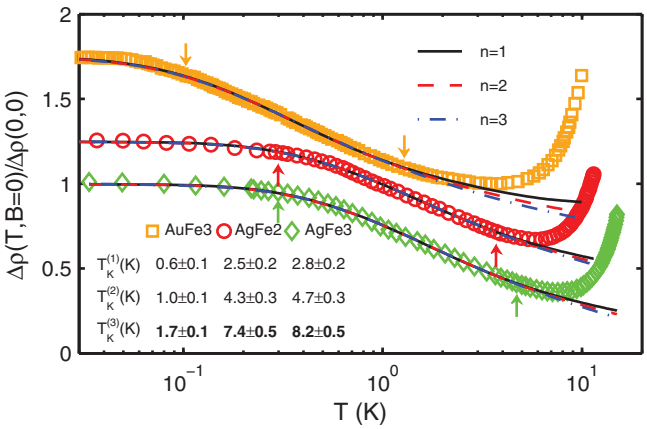

FIG. 3. (Color online) Similar figure as Fig. 3 of paper I, but using substantially improved numerical data. The figure shows low-field experimental data for the temperature dependence of the resistivity, denoted by $\Delta\rho^{\rm exp}(T,0)$ but taken in a small field of 0.1 T to suppress weak localization (see text), and NRG calculations for $n \in \{1,2,3\}$, performed at $B = 0$. The NRG curves were fitted to the experimental data, using $T_K^{(n)}$ and $\delta^{(n)}$ as fitting parameters [see Eq. (10)] with the fitting range being indicated by arrows. For temperatures below the fitting range, the data are less reliable due to a long equilibration time, whereas for temperatures above the fitting range the phonon contribution to $\Delta\rho^{\rm exp}(T, B = 0)$ becomes relevant. For clarity, the curves for AgFe2 and AuFe3 have been shifted vertically by 0.25 and 0.75, respectively.

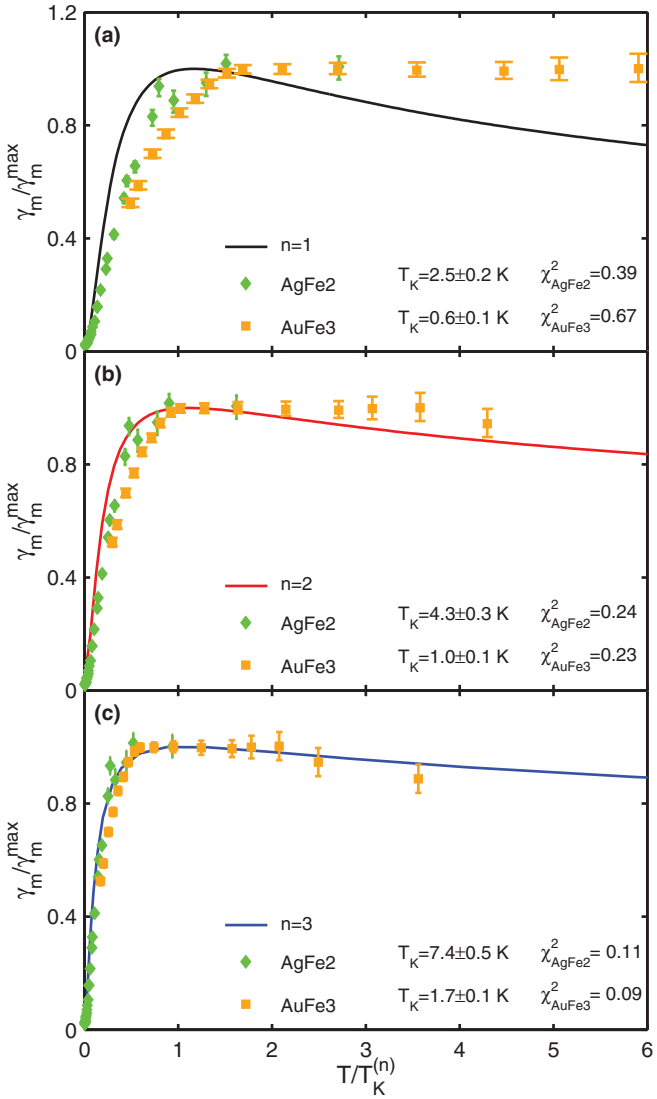

FIG. 4. (Color online) Similar figure as Fig. 4 of paper I, but using clearly improved numerical data. Panels (a), (b), and (c) show the normalized decoherence rate $\gamma_{\rm m}(T)/\gamma_{\rm m}^{\rm max}$ vs. $T/T_{\rm K}^{(n)}$ for $n \in \{1,2,3\}$, respectively. The Kondo temperatures are determined from the fits of $\rho_{\rm m}^{\rm NRG}(T, B=0)$ to the experimental data according to Eq. (10). The χ^2 values indicated in the legends were obtained as the sum of the least squares between the experimental data and the linearly interpolated NRG curves.

Here, $\rho_{\rm m}^{\rm exp}(T,B)$ is the resistivity due to magnetic impurities, $\rho_{\rm ph}(T)$ is the resistivity due to phonon scattering, and δ is an unknown offset which does not depend on temperature or magnetic field. There are two further contributions to the resistivity: a classical contribution,[8] which scales as B^2, and a contribution due to electron-electron interactions,[37,38] which scales as $1/\sqrt{T}$. These have already been subtracted from the measured resistivity data shown in Figs. 3 and 5 using procedures described in Refs. 39,40, and hence are not displayed in Eq. (9).

For the fitting process at $B = 0$, the normalized NRG data $\rho_{\rm m}^{\rm NRG}(T,0)/\rho_{\rm m}^{\rm NRG}(0,0)$ are approximated by a fitting function $g_n(T/T_{\rm K}^{(n)})$ constructed from higher-order polynomials, where $g_n(0) = 1$ and $T_{\rm K}^{(n)}$ is fixed by scaling the temperature axis such that $g_n(1) = \frac{1}{2}$ [cf. Eq. (8)]. We then fit the experimental data to the form

$$\Delta\rho^{\rm exp}(T,0) \approx \delta^{(n)} + (\Delta\rho^{\rm exp}(0,0) - \delta^{(n)}) g_n\left(T/T_{\rm K}^{(n)}\right), \quad (10)$$

using a χ^2 minimization with $T_{\rm K}^{(n)}$ and $\delta^{(n)}$ as fit parameters. While a similar analysis was performed in paper I, the numerical data in the present paper are of improved quality, in that we can report fully converged data also for the numerically extremely challenging case of $n = 3$. The newly extracted values of $T_{\rm K}^{(n)}$ for the three samples are given in Table I. For $n \in \{1,2\}$, they are slightly different from the ones of paper I, yet within the given error bars (14 % and 0 % for AuFe3, 9 % and 5 % for AgFe, respectively) due to the fact that we used different fitting ranges to minimize the error arising from the phonon-contribution for larger T and because we use higher-order polynomials to approximate the NRG data, which may be considered more accurate than the analytical expression used in paper I. The difference in $T_{\rm K}$ is more substantial for $n = 3$ (31 % for AuFe3 and 53 % for AgFe) reflecting larger differences between the previous and our new, improved NRG results for $n = 3$. Experimental and fitted NRG data are shown in Fig. 3.

B. Decoherence rate and magnetoresistivity

With the $T_{\rm K}^{(n)}$ for AgFe2 and AuFe3 determined above we are now in a position to make a parameter-free theoretical prediction of the decoherence rate. As shown in Fig. 4 for AgFe2 and AuFe3, the agreement is clearly best for $n = 3$ and becomes worse with decreasing n, both for low and high temperatures. A quantitative measure for the agreement is given by the χ^2 values for $n \in \{1,2,3\}$, which are displayed in each of the panels in Fig. 4. This conclusion is in accordance with paper I, where the $n = 3$ case also agreed best with the experimental data, although $T_{\rm K}$ and $\gamma_{\rm m}(T)$ for $n = 3$ were significantly less accurate then.

Next we turn to the magnetoresistivity. The above-mentioned implementation of non-Abelian symmetries in our NRG code,[15] which drastically reduces computation time and memory requirements, allows us to extend the analysis of $\rho_{\rm m}(T)$ of paper I to the whole two-dimensional parameter space of T and B. Since the fitting procedure of $\rho_{\rm m}(T, B = 0)$ described above leaves no further free parameters, this comparison is an additional strong check of the validity of the $n = 3$ model. The experimental data of $\rho_{\rm m}(T,B)$ for the sample AgFe2 are shown together with the numerical data for $n \in \{1,2,3\}$ in Fig. 5. [The values of $\rho_{\rm m}(T, B = 0)$ differ for $n \in \{1,2,3\}$, due to the different $\delta^{(n)}$ values determined from Eq. (10).] Again, the three-channel model reproduces the measured results best. Even though there are still slight deviations between theory and experiment at high magnetic field for the $n = 3$ curves at 0.1 and 0.85 K, which might originate from very small temperature drifts, the overall agreement, combined with that for $\gamma_m(T)$ (see Fig. 4) and $\rho_{\rm m}(T,0)$ (see Fig. 3), is rather impressive. Thus we conclude that the $n = 3$ model consistently reproduces all the transport data discussed above.

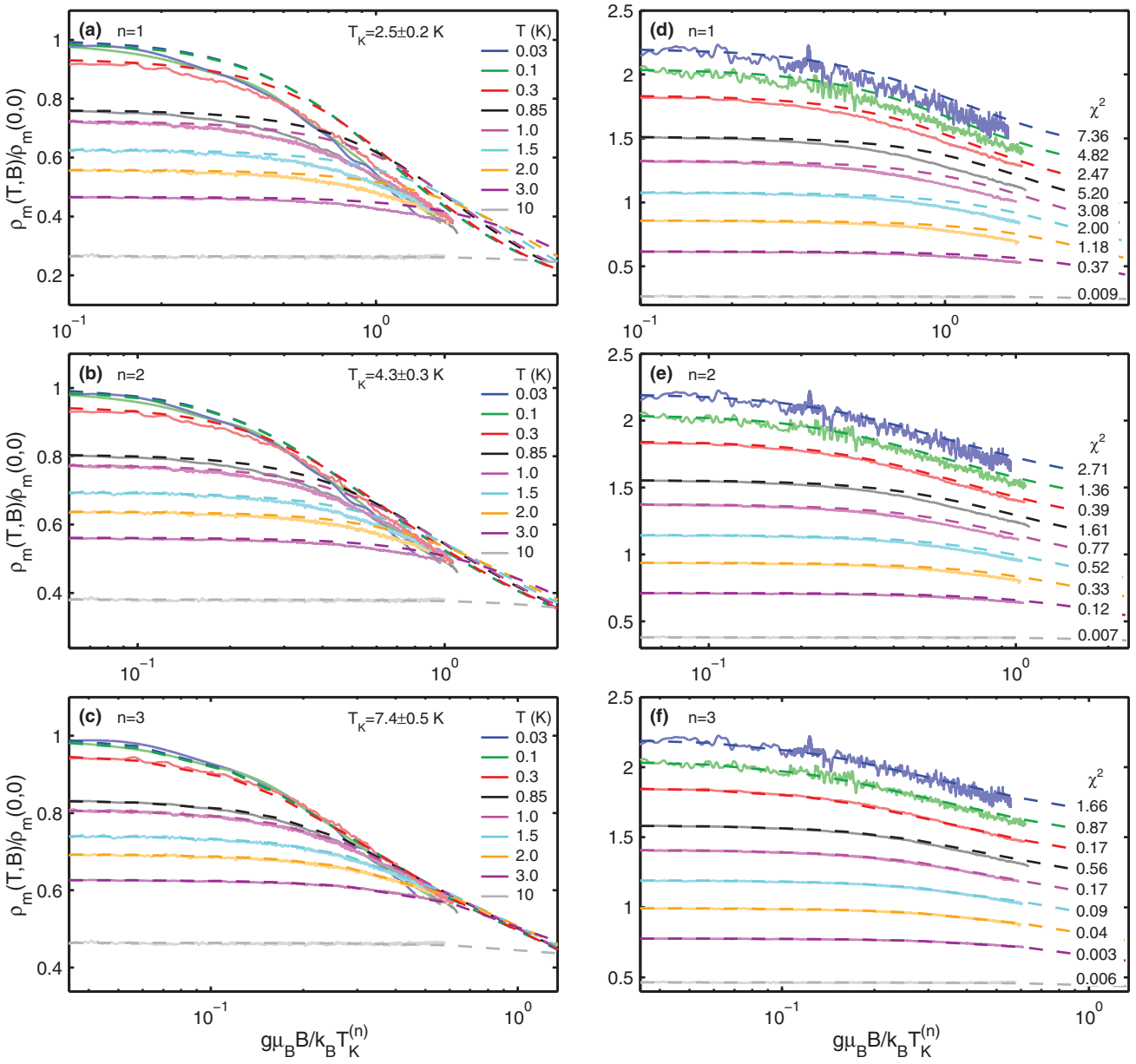

FIG. 5. (Color online) Experimental and theoretical results for $\rho_{\rm m}(T,B)$, shown using solid or dashed curves, respectively. Left column: (a), (b), and (c) compare the experimental data for AgFe2 to NRG-calculations for $n \in \{1,2,3\}$, respectively. Right column: (d), (e), and (f) show the same data as in the left column, except that for clarity the curves for successive temperatures are shifted vertically by 0.15 to avoid them from overlapping, thus enabling a better comparison between experiment and theory for each temperature. $T_{\rm K}^{(n)}$ and $\delta^{(n)}$ are already determined by the fitting procedure of Eq. (10), which allows a parameter-free theoretical prediction for $\rho_{\rm m}(T,B)$. The χ^2 values indicated in (d)–(f) were calculated using a set of 1000 uniformly spaced field values in the range $B \in [0.07349, 3.05000]$ T. The experimental data clearly show best agreement with theory for $n = 3$, which supports the conclusion from the examination of $\gamma_{\rm m}$. For $T = 0.030$ and 0.10 K, the signal to noise ratio is much lower than for the other curves since the measurement current had to be reduced to stay in thermal equilibrium; therefore in the left panels, the experimental data for these two temperatures have been smoothed for better visibility. For the largest temperature, $T = 10$ K, the phonon contribution has been subtracted from the experimental data for comparison to theory. For the purpose of this subtraction, the phonon contribution was assumed to be B-independent and taken to correspond to the difference of $\Delta\rho(T = 10K, B = 0)/\Delta\rho(0,0)$ between experiment and theory (see Fig. 3).

C. Channel anisotropy

To conclude this section, let us briefly discuss the possibility that the true effective Kondo model for Fe in Au and Ag could include some channel anisotropy. Channel anisotropy, if present at all, will be weak for the present system due to a symmetry argument. As mentioned in Introduction, Fe acts as substitutional defect in Au or Ag; it hence finds itself in an environment with cubic symmetry. This cubic symmetry protects the equivalence of the three local t_{2g} levels and of the three bands involved in the effective low-energy Kondo model. In particular, this cubic symmetry offers a rather strong protection against any splitting of the t_{2g} levels. A significant

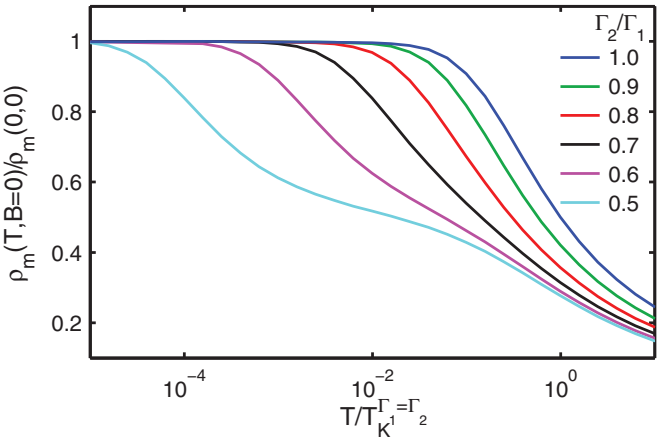

FIG. 6. (Color online) Temperature dependence of the resistivity for a channel-anisotropic Kondo model with $S = 1, n = 2$, for several different choices of Γ_2/Γ_1.

spin-orbit coupling, which could result in a spliting of the t_{2g} levels, was ruled out by density functional theory calculations in paper I.

With this in mind, let us nevertheless briefly discuss the possible effects of channel anisotropy, that could arise if some perturbation breaks the cubic symmetry. In general, such a perturbation could result in a small splitting in the n impurity d levels that yield the spin $n/2$, or in slightly different band widths or density of states for the n conduction-band channels, or in slightly different coupling strengths between local and band states in each channel. All of these will will have similar effects on the low-energy Kondo physics.

For concreteness, we consider here only the latter case, implemented in our model by setting $t \to t_\alpha$ in Eq. (1), leading to channel-dependent level widths $\Gamma_\alpha = \pi \nu_0 t_\alpha$. For a spin $n/2$, n-channel Kondo model, the presence of channel anisotropy quickly leads to a multistage Kondo effect,[10,14] characterized by n different Kondo temperatures $T_{K\alpha}$ in which channels of decreasing Γ_α successively screen the bare spin $n/2$ first to spin $(n-1)/2$, then to $(n-2)/2$, etc., down to 0. Since the corresponding Kondo temperatures $T_{K\alpha}$ depend exponentially on Γ_α, even a small amount of channel anisotropy changes the shape of the resistivity curve $\rho_m(T, B = 0)$ drastically. In particular, it spoils the purely logarithmic temperature dependence of the resistivity for $T \simeq T_K$, which is characteristic of the channel-isotropic Kondo effect: though each screening stage separately produces a logarithmic contribution to the resistivity, the sum of these contributions no longer behaves purely logarithmically, as illustrated in Fig. 6 for $n = 2$. Our experimental data, however, do not show signatures of such multistage Kondo physics. This implies that any channel anisotropy, if present, is weak. Therefore the differences between the various $T_{K\alpha}$-values associated with the successive stages of screening are, first, too small to be discernible in the data, and second, not at all required for the interpretation of the experimental data. We conclude that a fully channel-symmetric model suffices.

V. CONCLUSION

We have considered iron impurities in gold and silver and compared experimental data for the resistivity and decoherence rate to NRG results for a fully screened n channel, spin-$\frac{n}{2}$ Kondo model. Compared to previous work on this subject,[9] we showed improved numerical data for both quantities at finite temperature. In particular, we offered a detailed discussion of NRG convergence and truncation issues, using the discarded weight as a criterion for reliably judging the quality of convergence. Our most important new result is the analysis of the resistivity at finite magnetic field, where we compare the numerical calculations with as yet unpublished experimental data. In contrast to previous attempts to explain the experimental results with models with less channels which were inconsistent or yielded several different values for the Kondo temperature, depending on which set of measurements was used to extract T_K,[8] we showed that all examined quantities can be described consistently with a single value of T_K. The excellent agreement between experiment and theory for $n = 3$ shows that both systems are well described by a spin-3/2 three-channel Kondo model.

ACKNOWLEDGMENTS

We thank Norman Birge for helpful comments on the manuscript. We gratefully acknowledge financial support from ANR PNANO "QuSPIN" for L.S. and C.B., from the John von Neumann Institute for Computing (Jülich) for T.C., from WE4819/1-1 for A.W., and from SFB-TR12, SFB-631 and the Cluster of Excellence Nanosystems Initiative Munich for J.v.D., M.H., and A.W.

[1] W. J. de Haas, J. de Boer, and G. J. van den Berg, Physica **1**, 1115 (1934).
[2] W. J. de Haas and G. J. van den Berg, Physica **3**, 440 (1936).
[3] J. Kondo, Prog. Theor. Phys. **32**, 37 (1964).
[4] K. G. Wilson, Rev. Mod. Phys. **47**, 773 (1975).
[5] H. R. Krishna-murthy, J. W. Wilkins, and K. G. Wilson, Phys. Rev. B **21**, 1003 (1980).
[6] R. Bulla, T. A. Costi, and T. Pruschke, Rev. Mod. Phys. **80**, 395 (2008).
[7] F. Mallet, J. Ericsson, D. Mailly, S. Ünlübayir, D. Reuter, A. Melnikov, A. D. Wieck, T. Micklitz, A. Rosch, T. A. Costi, L. Saminadayar, and C. Bäuerle, Phys. Rev. Lett. **97**, 226804 (2006).
[8] G. M. Alzoubi and N. O. Birge, Phys. Rev. Lett. **97**, 226803 (2006).
[9] T. A. Costi, L. Bergqvist, A. Weichselbaum, J. von Delft, T. Micklitz, A. Rosch, P. Mavropoulos, P. H. Dederichs, F. Mallet, L. Saminadayar, and C. Bäuerle, Phys. Rev. Lett. **102**, 056802 (2009).
[10] P. Nozières and P. Blandin, J. Phys. **41**, 193 (1980).
[11] N. Andrei and C. Destri, Phys. Rev. Lett. **52**, 364 (1984).

[12]A. M. Tsvelik and P. B. Wiegmann, J. Stat. Phys. **38**, 125 (1985).
[13]I. Affleck, Nucl. Phys. B **336**, 517 (1990).
[14]I. Affleck, A. W. W. Ludwig, H.-B. Pang, and D. L. Cox, Phys. Rev. B **45**, 7918 (1992).
[15]A. Weichselbaum, Ann. Phys. **327**, 2972 (2012).
[16]A. I. Tóth and G. Zaránd, Phys. Rev. B **78**, 165130 (2008).
[17]A. I. Tóth, C. P. Moca, O. Legeza, and G. Zaránd, Phys. Rev. B **78**, 245109 (2008).
[18]A. Alex, M. Kalus, A. Huckleberry, and J. von Delft, J. Math. Phys. **52**, 023507 (2011).
[19]C. P. Moca, A. Alex, J. von Delft, and G. Zaránd, Phys. Rev. B **86**, 195128 (2012).
[20]R. Bulla, A. C. Hewson, and T. Pruschke, J. Phys.: Condens. Matter **10**, 8365 (1998).
[21]A. K. Mitchell, D. E. Logan, and H. R. Krishnamurthy, Phys. Rev. B **84**, 035119 (2011).
[22]We thank a referee for pointing out Ref. 21.
[23]B. Mühlschlegel, Zeitschrift für Physik **208**, 94 (1968).
[24]Y. Nishikawa and A. C. Hewson, Phys. Rev. B **86**, 245131 (2012).
[25]J. R. Schrieffer and P. A. Wolff, Phys. Rev. **149**, 491 (1966).
[26]T. Micklitz, A. Altland, T. A. Costi, and A. Rosch, Phys. Rev. Lett. **96**, 226601 (2006).
[27]G. Zarand, L. Borda, J. von Delft, and N. Andrei, Phys. Rev. Lett. **93**, 107204 (2004).
[28]A. Weichselbaum, Phys. Rev. B **84**, 125130 (2011).
[29]A. Weichselbaum and J. von Delft, Phys. Rev. Lett. **99**, 076402 (2007).
[30]F. B. Anders and A. Schiller, Phys. Rev. Lett. **95**, 196801 (2005).
[31]R. Peters, T. Pruschke, and F. B. Anders, Phys. Rev. B **74**, 245114 (2006).
[32]A. Weichselbaum, Phys. Rev. B **86**, 245124 (2012).
[33]D. C. Langreth, Phys. Rev. **150**, 516 (1966).
[34]M. Yoshida, M. A. Whitaker, and L. N. Oliveira, Phys. Rev. B **41**, 9403 (1990).
[35]L. Merker, S. Kirchner, E. Muñoz, and T. A. Costi, Phys. Rev. B **87**, 165132 (2013).
[36]The n-dependent differences in the shapes of the resistivity curve can be characterized in terms of analytic expressions for their asymptotic behavior at large and small ratios of $T/T_{\mathrm{K}}^{(n)}$ and $g\mu_{\mathrm{B}}B/k_{\mathrm{B}}T_{\mathrm{K}}^{(n)}$. Such an analysis would go beyond the scope of the present paper and will be published elsewhere.
[37]B. L. Altshuler and A. G. Aronov, in *Electron-Electron Interactions in Disordered Systems*, edited by A. L. Efros and M. Pollak (Elsevier, Amsterdam, 1985).
[38]E. Akkermans and G. Montambaux, *Mesoscopic Physics of Electrons and Photons* (Cambridge University Press, Cambridge, UK, 2007).
[39]C. Bäuerle, F. Mallet, F. Schopfer, D. Mailly, G. Eska, and L. Saminadayar, Phys. Rev. Lett. **95**, 266805 (2005).
[40]L. Saminadayar, P. Mohanty, R. A. Webb, P. Degiovanni, and C. Bäuerle, Physica E **40**, 12 (2007).